Earth Surf. Dynam., 11, 511–528, 2023
https://doi.org/10.5194/esurf-11-511-2023

Earth Surface Dynamics
Open Access
EGU

Feedbacks between the formation of secondary minerals and the infiltration of fluids into the regolith of granitic rocks in different climatic zones (Chilean Coastal Cordillera)

Ferdinand J. Hampl[1], Ferry Schiperski[1], Christopher Schwerdhelm[2], Nicole Stroncik[3], Casey Bryce[4], Friedhelm von Blanckenburg[3,5], and Thomas Neumann[1]

[1]Department of Applied Geochemistry, Technische Universität Berlin, Ernst-Reuter-Platz 1, 10587 Berlin, Germany
[2]Geomicrobiology Group, Eberhard Karl University of Tübingen, Schnarrenbergstrasse 94–96, 72076 Tübingen, Germany
[3]Earth Surface Geochemistry, GFZ German Research Centre for Geosciences, Telegrafenberg, 14473 Potsdam, Germany
[4]School of Earth Sciences, University of Bristol, Wills Memorial Building, Queens Road, Bristol BS8 1RJ, United Kingdom
[5]Institute of Geological Sciences, Freie Universität Berlin, Malteserstrasse 74–100, 12249 Berlin, Germany

Correspondence: Ferdinand J. Hampl (ferdinand.j.hampl@tu-berlin.de)

Received: 13 December 2022 – Discussion started: 17 January 2023
Revised: 11 May 2023 – Accepted: 16 May 2023 – Published: 22 June 2023

Abstract. Subsurface fluid pathways and the climate-dependent infiltration of fluids into the subsurface jointly control the intensity and depth of mineral weathering reactions. The products of these weathering reactions (secondary minerals), such as Fe(III) oxyhydroxides and clay minerals, in turn exert a control on the subsurface fluid flow and hence on the development of weathering profiles.

We explored the dependence of mineral transformations on climate during the weathering of granitic rocks in two 6 m deep weathering profiles in Mediterranean and humid climate zones along the Chilean Coastal Cordillera. We used geochemical and mineralogical methods such as (micro-) X-ray fluorescence (μ-XRF and XRF), oxalate and dithionite extractions, X-ray diffraction (XRD), and electron microprobe (EMP) mapping to elucidate the transformations involved during weathering. In the profile of the Mediterranean climate zone, we found a low weathering intensity affecting the profile down to 6 m depth. In the profile of the humid climate zone, we found a high weathering intensity. Based on our results, we propose mechanisms that can intensify the progression of weathering to depth. The most important is weathering-induced fracturing (WIF) by Fe(II) oxidation in biotite and precipitation of Fe(III) oxyhydroxides and by the swelling of interstratified smectitic clay minerals that promotes the formation of fluid pathways. We also propose mechanisms that mitigate the development of a deep weathering zone, like the precipitation of secondary minerals (e.g., clay minerals) and amorphous phases that can impede the subsurface fluid flow. We conclude that the depth and intensity of primary mineral weathering in the profile of the Mediterranean climate zone is significantly controlled by WIF. It generates a surface–subsurface connectivity that allows fluid infiltration to great depth and hence promotes a deep weathering zone. Moreover, the water supply to the subsurface is limited in the Mediterranean climate, and thus, most of the weathering profile is generally characterized by a low weathering intensity. The depth and intensity of weathering processes in the profile of the humid climate zone, on the other hand, are controlled by an intense formation of secondary minerals in the upper section of the weathering profile. This intense formation arises from pronounced dissolution of primary minerals due to the high water infiltration (high precipitation rate) into

the subsurface. The secondary minerals, in turn, impede the infiltration of fluids to great depth and thus mitigate the intensity of primary mineral weathering at depth.

These two settings illustrate that the depth and intensity of primary mineral weathering in the upper regolith are controlled by positive and negative feedbacks between the formation of secondary minerals and the infiltration of fluids.

1 Introduction

The formation of weathered material (regolith) from unweathered rock (bedrock) is a key process for shaping Earth's surface. It is of major importance for making mineral-bound nutrients accessible to the biosphere of the critical zone (e.g., Dawson et al., 2020) and to supply rocks and minerals to the sediment cycle. In this process, the in situ disaggregation and chemical depletion of weathered rock (saprock) to saprolite plays an essential role. This transformation is a result of fracturing and mineral dissolution (e.g., Navarre-Sitchler et al., 2015). Both are associated with chemical, physical (e.g., Goodfellow et al., 2016), and biological weathering processes (e.g., Drever, 1994; Lawrence et al., 2014; Napieralski et al., 2019). These processes are linked to climate-related parameters such as precipitation rate, fluid flow (water and gases), and biological activity. Apart from that, the weathering processes and hence the saprolite formation also depend on primary fractures (e.g., Molnar et al., 2007; Hynek et al., 2017; Kim et al., 2017; Holbrook et al., 2019; Hayes et al., 2020; Krone et al., 2021; Hampl et al., 2022a), discontinuity density and tortuosity (Israeli et al., 2021), thermoelastic relaxation (e.g., Nadan and Engelder, 2009), and the topographic surface profile (e.g., Rempe and Dietrich, 2014; St. Clair et al., 2015). However, one of the most fundamental parameters for the regolith formation is the mineral content of the bedrock. The weathering of some of these primary minerals and the consequent formation of secondary minerals can lead to an amplification of the depth and intensity (i.e., the parameter describing the elemental loss and relative amount of secondary minerals) of primary mineral weathering (e.g., Fletcher et al., 2006; Lebedeva et al., 2007; Buss et al., 2008; Behrens et al., 2015; Hampl et al. 2022a). Such mechanisms comprise (1) a forcing process like the formation of secondary minerals that is triggering (2) a responsive process such as more intense infiltration of fluids to depth. The latter process reinforces the initial forcing process of secondary mineral formation. Such a mechanism is therefore called positive feedback between (1) and (2). The formation of secondary minerals can also have a weathering-impeding effect (e.g., Lohse and Dietrich, 2005; Navarre-Sitchler et al., 2015; Kim et al., 2017; Gerrits et al., 2021) causing a mitigation of the weathering depth and intensity. Such mechanisms comprise (1) a forcing process like the formation of secondary minerals and (2) a responsive process such as reduced infiltration of fluids to depth. The latter process damps the initial forcing process of secondary mineral formation, and the mechanism is therefore called negative feedback between (1) and (2).

Deciphering the relationship between the formation of secondary minerals and the climatic conditions they were formed under is a prerequisite for understanding the weathering system. It allows us to determine whether feedbacks between the formation of secondary minerals and the infiltration of fluids affect the intensity and depth of primary mineral weathering. We hypothesize that a positive feedback loop results in a deep weathering depth as secondary minerals form fluid pathways by fracturing due to volume increase. On the other hand, we think that a negative feedback loop leads to a shallow weathering depth as the precipitation of secondary minerals seals fluid pathways.

To explore such connections and to elucidate the impact of secondary minerals on the development of weathering systems in different climatic zones, we investigated two 6 m deep weathering profiles in the Chilean Coastal Cordillera. One profile is located in a Mediterranean climate zone (mean annual temperature: 14.9 °C, mean annual precipitation: 436 mm yr^{-1}) and another in a humid climate zone (mean annual temperature: 14.1 °C, mean annual precipitation: 1084 mm yr^{-1}) (Scheibe et al., 2023), and both developed from the weathering of granitic rock. Both sites are eroding and the surfaces in the locations are thus constantly turned over (see compilation of rates and environmental parameters in Oeser and von Blanckenburg (2020) and references therein). The profiles were sampled in soil pits and complemented with rock samples obtained by deep wireline rotary drilling close to the soil pits. Samples were investigated by a combination of analytical techniques such as X-ray fluorescence (XRF), micro-X-ray fluorescence (μ-XRF), and oxalate and dithionite extraction, which are used to characterize the geochemical composition, and X-ray diffraction (XRD), magnetic susceptibility measurements, electron microprobe (EMP), and light microscopy, which are used to identify the mineral assemblages. The combined results of these techniques are used to derive weathering-intensifying and -mitigating processes during subsurface weathering and to elucidate how these processes influence the depth and intensity of weathering in the different climate zones.

2 Study sites

2.1 La Campana (LC)

The soil pit (−33.02833° N, −71.04370° E, 894 m) and the drilling site some 15 m next to it (−33.02833° N, −71.04354° E, 898 m) are located south of the La Campana National Park approximately 60 km NW of Santiago de Chile (Fig. 1a). They are situated on a ridge with steep slope dip angles of 20–30°.

The vegetation can be characterized as Mediterranean sclerophyllous forest with *Cryptocarya alba* and *Lithraea caustica* as dominant plants (Luebert and Pliscoff, 2006; Oeser et al., 2018; Fig. 1b, c). The annual precipitation rate (measured from April 2016 to April 2020) is 346 mm yr^{-1} (Übernickel et al., 2020), and the Holocene net primary production is 280 ± 50 g C m^{-2} yr^{-1} (Werner et al., 2018; Oeser and von Blanckenburg, 2020). Records of long-term meteorological data (e.g., precipitation at ground level, soil water content, air temperature, relative humidity) from a weather station near the study site can be found in Übernickel et al. (2020).

The regolith profile developed on top of Upper Cretaceous intrusions of mainly granodiorites and tonalites with subordinate quartz monzodiorites (Gana et al., 1996). The depths of the soil horizons are as follows: A – 0–30 cm, B – 30–83 cm, and C (saprolite) – > 83 cm (Fig. 1d). Uplift rates for the north of Santiago de Chile vary between 0.01 and 0.23 mm yr^{-1} with a general mean value of 0.13 ± 0.04 (Melnick, 2016). The soil denudation rate in the nearby La Campana National Park is 53.7 ± 3.4 (S-facing slope) to 69.2 ± 4.6 t km^{-2} yr^{-1} (N-facing slope) (Oeser et al., 2018), or assuming a material density of 2.6 g cm^{-3}, 0.024 mm yr^{-1} on average.

2.2 Nahuelbuta (NA)

The investigated soil pit (−37.79371° N, −72.95065° E, 1113 m) and the drilling site next to it (−37.79381° N, −72.95043° E, 1114 m) are located approximately 20 km west of Angol (Region IX (Araucanía), Malleco Province) in southern Chile (Fig. 1a). The borehole was located on a plateau-like ridge with gently dipping slopes (ca. 10°).

The pre-land-use vegetation in the study area resembled the recent vegetation found in the Nahuelbuta National Park which can be characterized as temperate forest with *Araucaria araucana* as the dominant tree (Luebert and Pliscoff, 2006; Fig. 1e). However, extensive modern pastoral farming (cow grazing) and fires have converted the ecosystem in the study area to a sparse forest of deciduous trees such as *Nothofagus obliqua* (see Oeser et al., 2018; Fig. 1f). Numerous signs of burning can be observed in the field and charcoal is an integral component of the soil down to 25 cm (A horizon). The precipitation rate (measured from the end of March 2016 to April 2020) is 1927 mm yr^{-1} (Übernickel et al., 2020) and the Holocene net primary production is 520 ± 130 g C m^{-2} yr^{-1} (Werner et al., 2018; Oeser and von Blanckenburg, 2020). Records of long-term meteorological data (e.g., precipitation at ground level, soil water content, air temperature, relative humidity) from a weather station near the study site can be found in Übernickel et al. (2020).

The regolith profile developed on top of granitoid rocks of the Nahuelbuta central pluton which contains heterogenous lithological portions (Hervé, 1977; Ferraris, 1979). It is part of the Nahuelbuta Batholith which in turn belongs to the Late Carboniferous Chilean Coastal Batholith (Steenken et al., 2016; Deckart et al., 2013). The depths of the soil horizons are as follows: A – 0–25 cm, B – 25–90 cm, and C (saprolite) – > 90 cm (Fig. 1g). Today's exhumation rates in NA are high (> 0.2 mm yr^{-1}; Glodny et al., 2008b), whereas the catchment-wide denudation rate is small (27.4 ± 2.4 mm kyr^{-1}; van Dongen et al., 2019) compared to LC. The soil denudation rate in the nearby Nahuelbuta National Park ranges between 17.7 ± 1.1 (N-facing slope) to 47.5 ± 3.0 t km^{-2} yr^{-1} (S-facing slope) (Oeser et al., 2018), or assuming a material density of 2.6 g cm^{-3}, 0.013 mm yr^{-1} on average. Tectonic fractures in NA can be related to the Lanalhue Fault Zone (see Glodny et al., 2008a).

3 Materials and methods

3.1 Soil pit sampling, drilling, and sample preparation

The sampled 6 m deep soil profiles were located close to the main boreholes at the respective sites. Bulk samples were collected in 20 intervals in each soil pit and weighed around 3 kg. Corestones were not encountered in the soil pit profiles of LC and NA. By using a rotary splitter (type PT, Retsch) the bulk samples were separated into aliquots (see Hampl et al., 2022b). During the drilling campaigns, up to 1.5 m long core runs were recovered by wireline diamond drilling (∼ 80 mm core diameter) using potable water as drilling fluid (see Krone et al., 2021 for a detailed description of the drilling technique). Rock samples were separated from the core by mechanical methods (angle grinder, hammer, and chisel), cut (diamond saw), impregnated with blue artificial resin filling the porosity, and subsequently thin-sectioned. Representative bedrock samples were separated from the core (diamond saw) and crushed (jaw crusher).

3.2 Analytical methods and calculations

A detailed description of the analytical methods can be found in the accompanying data publication of this study (Hampl et al., 2022b).

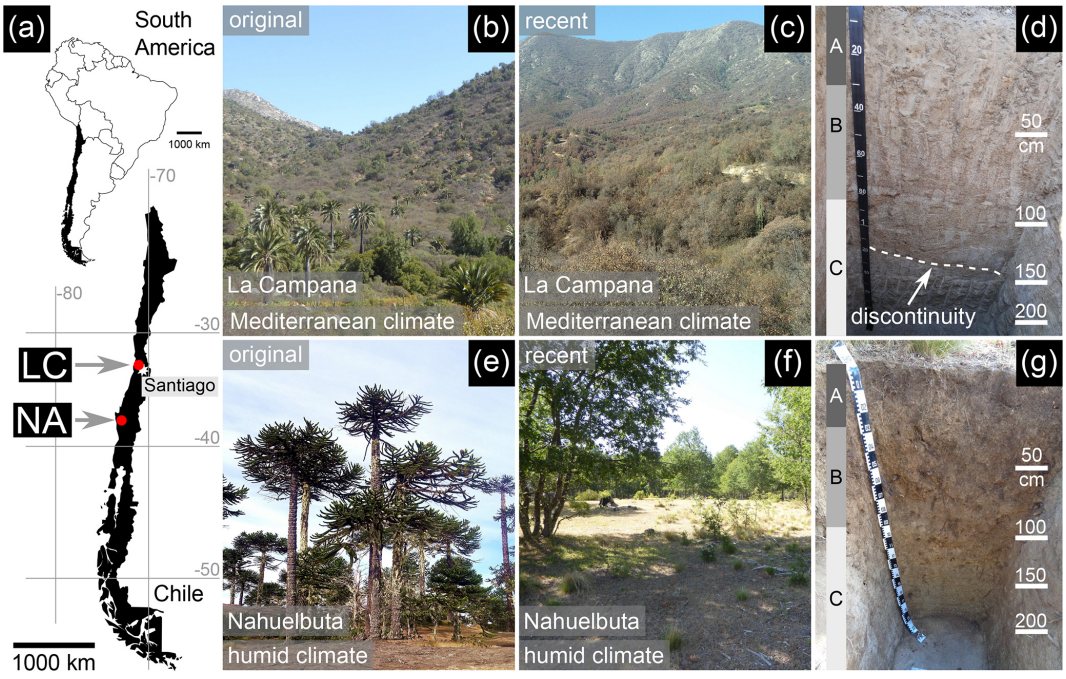

Figure 1. Overview of the study sites and soil profiles. **(a)** Position of La Campana (LC) and Nahuelbuta (NA) in Chile. Modified map data from OpenStreetMap (© OpenStreetMap contributors). **(b)** Original vegetation in LC (i.e., before human intervention; La Campana National Park). **(c)** Vicinity of the soil pit and drilling site in LC and **(d)** the first 2 m of the soil profile in LC with inscribed soil horizons (A–C). A prominent discontinuity (dashed line) can be found in the depth interval of 120–140 cm. **(e)** The original vegetation in NA (i.e., before human intervention; Nahuelbuta National Park) in comparison to **(f)** the recent vegetation in the vicinity of the soil pit and drilling site. **(g)** The first 2 m of the soil profile in NA with inscribed soil horizons (A–C).

3.2.1 X-ray fluorescence (XRF) and micro-X-ray fluorescence (μ-XRF)

Soil pit samples were ground with an agate disk mill and annealed (950 °C for 1 h) before adding a lithium borate flux to produce glass beads in platinum crucibles. The element composition of the glass beads was analyzed with a Thermo Scientific ARL PERFORM'X X-ray fluorescence sequential spectrometer (WD-XRF; Thermo Fisher Scientific Inc., USA). Additional powder pellets were produced by mixing the ground air-dried samples with wax. The mixtures were pressed and analyzed with a SPECTRO XEPOS energy dispersive X-ray fluorescence spectrometer (ED-XRF, SPECTRO Analytical Instruments GmbH, Germany). Polished sample slabs of bedrock (Fig. 2) were mapped for the spatial distribution of elements with a μ-XRF spectrometer M4 Tornado (Bruker, Germany).

Geochemical calculations

Zr contents obtained from the XRF element analyses on powder pellets were used as an immobile element for the calculation of the chemical depletion fraction (CDF; Riebe et al., 2003; Eq. 1) and the mass transfer coefficient (τ; Anderson et al., 2002; Eq. 2).

$$\mathrm{CDF} = 1 - \frac{\mathrm{Zr_N^b}}{\mathrm{Zr_N^w}}, \tag{1}$$

$$\tau = \frac{X^{\mathrm{w}} \cdot \mathrm{Zr}^{\mathrm{b}}}{X^{\mathrm{b}} \cdot \mathrm{Zr}^{\mathrm{w}}} - 1, \tag{2}$$

where X^{b} is the concentration of element X in the bedrock, X^{w} is the concentration of element X in the weathered sample, Zr^{b} is the concentration of Zr in the bedrock, $\mathrm{Zr_N^b}$ is the zirconium content of the bedrock normalized to a LOI-free (loss-on-ignition-free) sum of 100 % (see Hampl et al., 2022b), Zr^{w} is the concentration of Zr in the weathered sample, and $\mathrm{Zr_N^w}$ is the zirconium content of the weathered sample normalized to a LOI-free sum of 100 % (see Hampl et al., 2022b).

The chemical index of alteration (CIA; Nesbitt and Young, 1982) was modified to ΔCIA (Eq. 3).

$$\Delta\mathrm{CIA} = \left[\left(\frac{\mathrm{Al_2O_3}^{\mathrm{w}}}{\mathrm{Al_2O_3}^{\mathrm{w}} + \mathrm{CaO}^{\mathrm{w}} + \mathrm{Na_2O}^{\mathrm{w}} + \mathrm{K_2O}^{\mathrm{w}}}\right) - \left(\frac{\mathrm{Al_2O_3}^{\mathrm{b}}}{\mathrm{Al_2O_3}^{\mathrm{b}} + \mathrm{CaO}^{\mathrm{b}} + \mathrm{Na_2O}^{\mathrm{b}} + \mathrm{K_2O}^{\mathrm{b}}}\right)\right] \cdot 100, \tag{3}$$

where superscript w means in the weathered sample and superscript b means in the bedrock.

3.2.2 Oxalate and dithionite extractions

Air-dried bulk samples of < 2 mm (dry sieved) were used for oxalate and dithionite extractions. The solutions thus obtained were measured with an ICP-OES iCAP 6300 DUO (Thermo Fisher Scientific, USA) to determine the extractable Fe, Al, and Si contents. The oxalate extraction employed targets the easily extractable, mainly X-ray amorphous Fe(III) oxyhydroxides and (poorly) crystalline Al-containing minerals (see review by Rennert, 2019 and references therein). The dithionite extraction dissolves crystalline and amorphous iron oxides (McKeague and Day, 1966). In doing so, it can (partly) attack Al-bearing (mineral) phases (see review by Rennert, 2019 and references therein).

The oxalate extractions were performed after Schwertmann (1964) with an oxalic acid/oxalate extraction solution (0.2 M, pH 3.0). After the addition of the solution to the sample and shaking for 2 h in the dark (overhead shaker), the solution was filtered in a darkened room and immediately measured. The cold dithionite extractions were performed based on Holmgren (1967) with an extraction solution (mixture of 0.2 M $NaHCO_3$ and 0.24 M trisodium citrate) and sodium dithionite under oxic conditions. The resulting mixture of chemicals and sample was shaken for 16 h and centrifuged before the supernatant was filtered and immediately measured. Additional reference samples, blanks, and calibration solutions were also prepared and measured like the soil pit samples. The results of the samples presented here are the mean of duplicate measurements performed on two individually extracted sample aliquots.

3.2.3 Grain size determination

Sample aliquots were suspended in deionized water ($< 10\,\mu S\,m^{-1}$) and dispersed in a rotating overhead shaker (approximately 15 h) and a subsequent ultrasonic bath before vibrational wet sieving. The > 63 µm sieving fractions were dried (50 °C, approximately 24 h) and their weight percentages were measured. The clay and silt contents were determined using the < 63 µm suspension and a pipette method. Organic-rich samples were treated with H_2O_2 to decompose organic matter, and sodium pyrophosphate was used as a dispersion agent to prevent coagulation. Clay (< 2 µm) was separated from the < 63 µm fraction slurry via centrifugation.

3.2.4 X-ray diffraction (XRD)

Untreated air-dried aliquots of bulk samples were crushed in a porcelain mortar and then processed with a micronizing XRD-mill McCrone (Retsch, Germany) to obtain a final powder of < 10 µm. These powders were mounted to XRD sample holders by backloading, and X-ray diffraction measurements were performed with a Rigaku SmartLab equipped with a 9 kW rotating Cu anode and a HyPix-3000 detector in Bragg–Brentano geometry (3–80° 2θ, scan step: 0.01°, scan speed: $1°\,min^{-1}$, and 60 rpm sample rotation). For the identification and semiquantitative analyses, the software SmartLab Studio II and the mineral database PDF-4 Minerals 2021 including reference intensity ratio (RIR) factors were used. Image processing (imageJ, version 1.53a; Schneider et al., 2012) performed on the μ-XRF element distribution maps in Fig. 2 was used to get rough compositional information of the mineral content in the sampled bedrock. These analyses were used as a supporting basis for the semiquantitative XRD analyses with RIR factors.

Clay mineral contents in the samples were quantitatively estimated by combining the results of the grain size determination with the semiquantitative results of the XRD analyses. The clay-size fraction (< 2 µm) of which the mass was determined by sieving/pipetting, was assumed to represent the entire clay mineral content of the sample, while the other size fractions were considered to be free of clay minerals. This assumed clay mineral content (in wt %) was combined with the XRD-semiquantitative weight percentages of the primary minerals in the same sample to approximate the mineral composition of the whole soil pit sample (summarized to 100 wt %). Despite the assumption that only the < 2 µm grain size fraction contains clay minerals, this estimate appears to be the most accurate because there are no matching files in the mineral database used here that would accurately semiquantify the identified interstratified clay minerals.

The separated clay-size fractions were measured as oriented clay films (texture preparation). A D2 Phaser XRD device (Bruker) equipped with a Cu anode was utilized for the measurements. The diffractograms were recorded in Bragg–Brentano geometry in the range of 3–35° 2θ (step width: 0.01° 2θ, 0.5 s per step). The samples were measured after air-drying, during ethylene glycol saturation, and after a thermal treatment at 550 °C for 1 h. Selected samples were also treated with glycerol and KCl (1 M) to characterize the clay minerals in more detail. The identification was supported by a clay mineral identification chart (Starkey et al., 1984).

3.2.5 Magnetic susceptibility measurements

The magnetic susceptibility was measured on all 21 McCrone-milled bulk samples of the LC profile with a KLY-3 Kappabridge (AGICO, Czechia). Measurements were performed in triplicates at room temperature, at a frequency of 875 Hz, and a peak magnetic field of $300\,A\,m^{-1}$.

To obtain the magnetite content of the bedrock, a representative $60 \times 60\,mm$ sample slab (Fig. 2a) was mapped with the μ-XRF spectrometer M4 Tornado. The μ-XRF map that depicts only the maximum Fe content was used as an approximation of the magnetite content since magnetite is the mineral with the highest Fe concentration in the rock. Finally, the map was analyzed with the image-processing program imageJ (version 1.53a; Schneider et al., 2012) to quantify the magnetite content. The obtained value was equalled to the measured magnetic susceptibility of the same sample and used to convert the magnetic susceptibility results of the LC

soil pit samples into approximated magnetite contents by the rule of three. The investigated bedrock of NA contains no magnetite.

3.2.6 Light microscopy and electron microprobe analysis (EMPA)

Thin sections were investigated with the light microscope DM750P (Leica, Wetzlar, Germany) equipped with a microscope camera (Euromex, The Netherlands). Electron microprobe element distribution maps of selected areas were obtained for Al, Ca, Fe, K, and Mg by using standard wavelength dispersive techniques on a JEOL Superprobe JXA-8230 fitted with a W-emitter electron gun (accelerating voltage: 15 kV, beam current: 20 nA, beam diameter and step width: 1 µm).

4 Results

The data tables (cited as Tables S1–S5) are included in the accompanying data publication (Hampl et al., 2022b).

4.1 Bedrock

According to the Streckeisen nomenclature, the bedrock of LC can be described as granodiorite, and the investigated bedrock of NA can be described as granite. However, the drill core revealed that the bedrock of NA occasionally contains more mafic sections. The most abundant minerals in the fine-grained bedrock of LC are plagioclase, quartz, microcline, hornblende, biotite, and chlorite (Fig. 2a, b). The latter occurs solely and abundantly along with (former) biotite crystals as their hydrothermal transformation products (i.e., chloritization; e.g., Kogure and Banfield, 2000). Magnetite is a ubiquitous accessory mineral (Fig. 2c; < 1 vol. %) in LC and shows no signs of alteration to hematite (martitization). Pyrite and chalcopyrite are also observed in much smaller abundance than magnetite. Mafic xenoliths can frequently be found in the granodiorite of LC.

In the coarse-grained Nahuelbuta granite, quartz, plagioclase, microcline, biotite, and chlorite are the main constituents (Fig. 2d, e). In contrast to LC, amphiboles can only be found as an accessory mineral (< 1 vol. %) in the investigated bedrock of NA. Like in LC, biotite is often chloritized. Magnetite and sulfides could not be identified in the investigated rock samples of NA. Variations in the biotite content, the occurrence of amphibole crystals, differences in fabric (microcline of a few centimeters), the alternation with mafic portions, and the presence of pegmatites in the core make the overall lithology of NA far more heterogenous compared to LC.

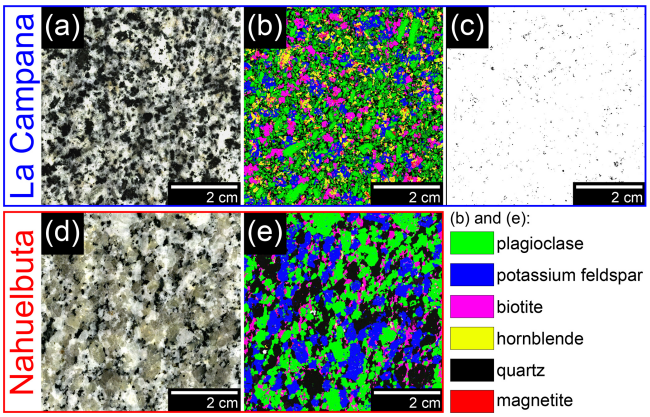

Figure 2. Bedrock of the investigated profiles. **(a)** Bedrock from La Campana (IGSN: GFFJH0095) with **(b)** a corresponding μ-XRF map reflecting the spatial mineral distribution. **(c)** A μ-XRF map of the maximum Fe content (black dots) representing the magnetite crystals in the bedrock sample slab of La Campana. **(d)** Typical unweathered granite from Nahuelbuta (IGSN: GFFJH00H0) and **(e)** a μ-XRF map reflecting the mineral content of the same.

4.2 Regolith

4.2.1 Incipient weathering in rock

Weathered rock from the borehole of LC shows abundant indications of weathering-induced fracturing (WIF) due to Fe(II) oxidation in biotite, like fanned-out edges or opening due to dilatation (Fig. 3a, b). Secondary minerals like Fe(III) oxyhydroxides are subordinate and are mostly associated with biotite. They are detectable as Fe enrichments at the edge of biotite crystals and within the cracks encompassing biotite (Fig. 3c, d). To a minor degree, Fe(III) oxyhydroxides are also associated with hornblende. Nevertheless, most microfractures in feldspar and quartz of the investigated thin sections are solely filled with blue resin and are bare of any secondary minerals.

Indications of WIF around biotite are also present in weathered rock of NA (Fig. 4a, b). However, the cracks are often filled and covered with Fe(III) oxyhydroxides and clay minerals as observed with light microscopy (Fig. 4c) and electron microprobe investigations. Unlike LC, weathered rock in NA is characterized by distinct Ca-depletion and Alenrichment in plagioclase which indicates partial dissolution (Fig. 4d–f). These alteration sites host secondary minerals covering the newly formed surfaces which were formed by the dissolution of the plagioclase.

4.2.2 Saprolite and soil

Chemical alteration

The mass transfer coefficient τ indicates moderate depletion below 80 cm (not smaller than -0.2) in the LC soil pit profile but clear depletion in the uppermost few decimeters where

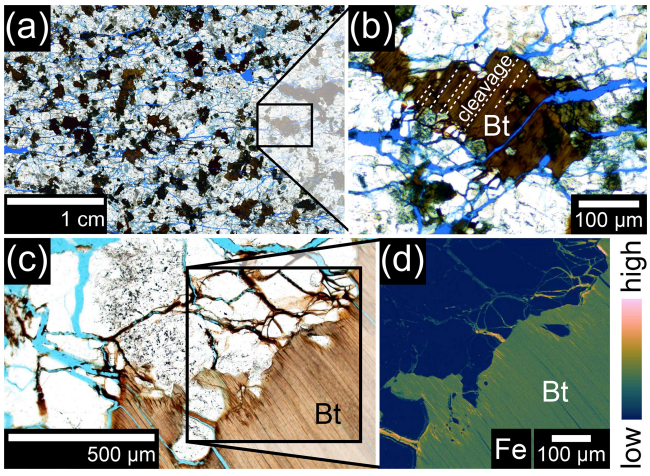

Figure 3. Rock weathering in La Campana (LC; porosity is represented by blue-dyed resin). **(a)** Thin section image (transmitted light) of a weathered rock sample obtained from a depth of approximately 27 m in the LC drill core (IGSN: GFFJH00HY). **(b)** A detail image of biotite showing signs of dilatation (dashed lines indicate cleavage planes). **(c)** Secondary minerals in cracks around biotite. **(d)** The electron microprobe map of the contact zone between biotite and quartz/feldspar displays Fe enrichments at the interface. Bt denotes biotite.

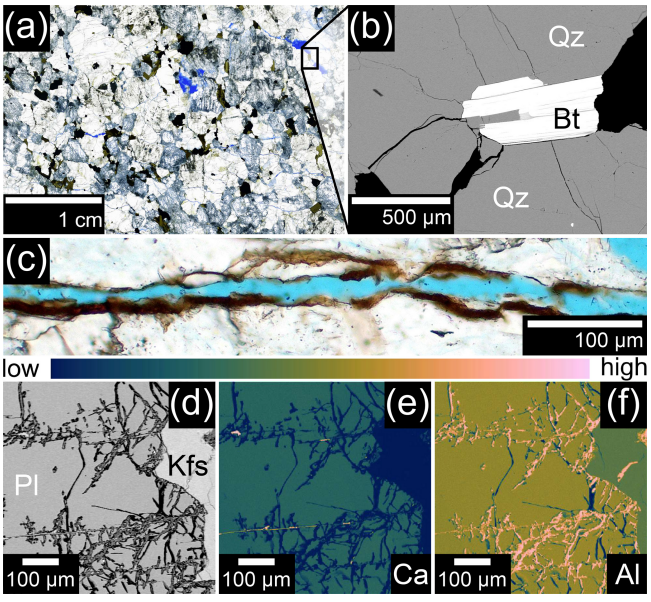

Figure 4. Rock weathering in Nahuelbuta (NA). **(a)** Thin section image (transmitted light) of weathered rock obtained from approximately 6 m depth in the NA drill core (note that the porosity (blue) is largely associated with weathered plagioclase; IGSN: GFFJH00HX). **(b)** Indications of WIF in quartz (backscattered electron image, EMP). **(c)** Thin section image (transmitted light) of a crack covered with brown Fe(III) oxyhydroxides from a depth of approximately 12 m (IGSN: GFFJH00J2). **(d)** Backscattered electron image (EMP) of partly dissolved plagioclase and **(e)** the respective Ca and **(f)** Al map of the section (IGSN: GFFJH00HX). Qz denotes quartz, Bt denotes biotite, Pl denotes plagioclase, and Kfs denotes potassium feldspar.

Na, K, Mg, Ca, Si, and P can reach up to $\tau = -0.5$ and -0.6 (Fig. 5; Table S1). A pronounced P depletion can be detected down to a depth of 1.4 m in LC. The chemical depletion fraction (CDF) of LC and the bedrock-normalized chemical index of alteration (ΔCIA) indicate a weak chemical weathering degree below ca. 0.5–1 m, but minor chemical depletion was analyzed down to the bottom of the 6 m deep profile of LC (see ΔCIA; Fig. 5).

In contrast, Nahuelbuta is characterized by distinct chemical depletion of Ca and Na (up to $\tau = -0.9$; Fig. 5). K is depleted to a depth of approximately 5 m, Si to a depth of $\sim$ 6 m, and Mg shows moderate depletion ($\tau \geq -0.3$) throughout the profile. P is strongly depleted between ca. 2–6 m ($\tau \sim -0.6$) but the P content gradually increases from a depth of approximately 3 m towards the surface and is enriched in the uppermost $\sim$ 20 cm of the soil (A horizon; Fig. 5). The CDF values of NA indicate depletion down to the bottom of the profile at a depth of 6 m. The ΔCIA of the profile underpins strong chemical alteration compared to the bedrock (Fig. 5). However, overall chemical depletion decreases towards the bottom of the soil profile and according to the τ values in 550–600 cm, only Na, Ca, and P seem to be significantly depleted at a depth > 6 m.

Since many secondary minerals are formed via a metastable or amorphous precursor (e.g., Steefel and van Cappellen, 1990; Hellmann et al., 2012; Behrens et al., 2021), we assume that the extractable Fe, Si, and Al contents are indicative of recent weathering of primary minerals (Fig. 6; see Sect. 3.2.2 for an assignment of the extractable elements to the minerals they likely originate from).

Extractable contents of Fe in LC are moderately elevated in the uppermost meter of the profile (up to $Fe_{dit} / Fe_{tot} \sim 14\,\%$) compared to the other depth intervals which show low contents ($Fe_{dit} / Fe_{tot} < 1$ m: $\sim 4\,\%$–$5\,\%$; Table S2; Fig. 6a, b). The extractable Si contents show no clear pattern (Fig. 6c, d), whereas oxalate- and dithionite-extractable Al contents are variable in the profile of LC (Fig. 6e, f). The elevated Al_{did} / Al_{tot} value in the depth interval of 120–140 cm in LC ($\sim 0.5\,\%$; Fig. 6f) coincides with a discontinuity in the saprolite (Fig. 1d) and may indicate more secondary crystalline and amorphous Al-bearing phases in this section. The profile in NA is characterized by high amounts of extractable Fe, Si, and Al contents which are especially elevated in the uppermost meter of the profile (Fe_{dit} / Fe_{tot} up to $\sim 40\,\%$, Si_{dit} / Si_{tot} up to $\sim 0.14\,\%$, Al_{dit} / Al_{tot} up to $\sim 12\,\%$). The extractable contents rapidly decrease from the surface towards the bottom of the NA profile and starting at approximately 2 m, they are similar down to 6 m (Fig. 6).

The Fe_2O_3 content in the investigated bedrock of LC is more than twice as high as that of the NA bedrock, but the

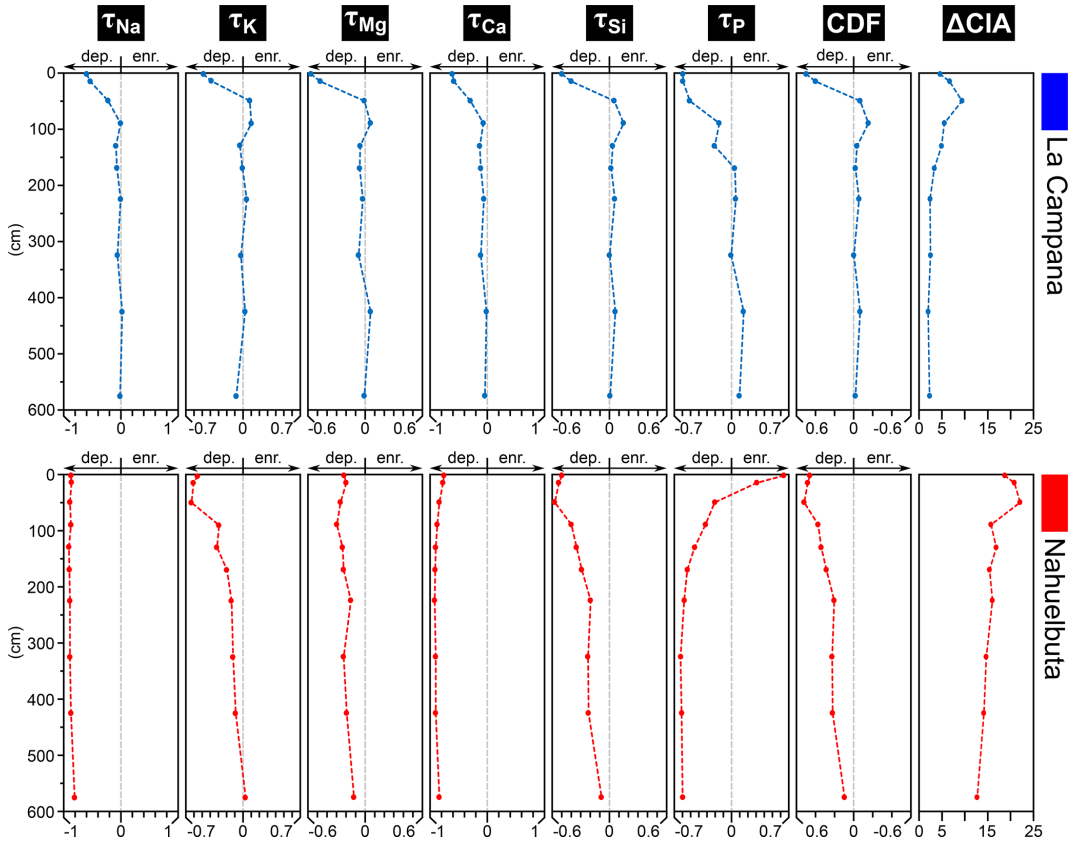

Figure 5. τ values of Na, K, Mg, Ca, Si, and P as well as the CDF (all based on Zr) and ΔCIA values of the soil pit profiles in La Campana (LC) and Nahuelbuta (NA; Table S1). Note that the scales are equal for the individual indices of LC and NA; dep. denotes depletion and enr. denotes enrichment.

oxalate- and dithionite-extractable Fe contents (and hence the amount of the respective secondary minerals) are far higher in NA (Fig. 6a, b). The difference between LC and NA is even more pronounced for the extractable Al contents as values in NA can be 10 times higher than in LC (Fig. 6e, f). The extractable contents in the profiles of both study sites are generally within the range of previous investigations on soil samples from the La Campana and Nahuelbuta National Parks, but the Fe_{dit} / Fe_{tot} contents in the upper profile section of NA in this study are much higher (up to 40 %) than those measured in the Nahuelbuta National Park (< 25 %; Oeser et al., 2018).

Mineral content and grain sizes

The sieving results of LC show a gradual decrease in particle size from the bottom of the profile towards the surface and a relatively constant sand-size content ranging from 65 wt %–80 wt % with similar portions of the individual sand-size fractions (Fig. 7a). The small geochemical depletion below the uppermost ~ 2 m of the LC profile (Fig. 5) is also reflected in the little changing mineral composition of the profile (Fig. 7b). Only the plagioclase (Ca–albite) content slightly decreases from a depth of approximately 1 m towards the surface. A small decrease of biotite in the depth interval of 120–140 cm coincides with the mentioned discontinuity of this profile section (Fig. 1d). The abundant chlorite of the investigated bedrock in LC (~ 5 wt %) is completely weathered and absent from the soil pit samples (Fig. 7b).

Significant alteration of magnetite (e.g., martitization) could not be observed in ore microscopic investigations of the magnetic particles in soil pit samples of LC. Thus, the magnetic susceptibility directly reflects the magnetite content of the samples (e.g., Ferré et al., 2012). A relative magnetite enrichment was detected in the uppermost 40 cm of the LC profile (1–1.6 vol. %), whereas the rest of the profile shows approximately constant magnetite contents (mean ~ 0.9 vol. %) close to the value of the investigated bedrock (0.94 vol. %; Fig. 7c). This almost consistent magnetite content underlines the homogeneity of the bedrock that was weathered in the 6 m deep soil pit (i.e., no mafic dikes, pegmatites, or major xenoliths).

The soil pit profile of NA is characterized by a much higher gravel-, silt-, and clay-size content compared to LC (Fig. 7d). This reflects the more heterogeneous grain size distribution of the investigated bedrock in NA compared to

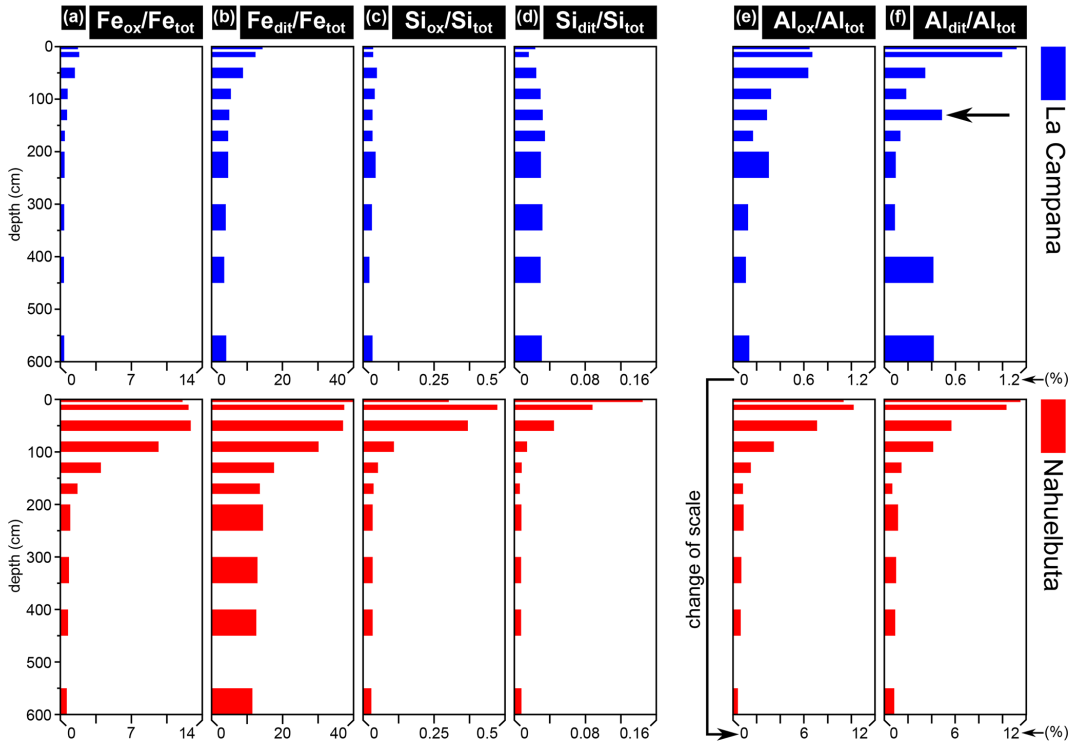

Figure 6. Oxalate- and dithionite-extractable Fe, Si, and Al contents divided by the respective total element contents of the bulk soil pit samples of La Campana (LC) and Nahuelbuta (NA; Table S2). The elevated ratio at 120–140 cm in **(f)** (arrow) coincides with the position of a discontinuity in the profile (Fig. 1d). Note that the scales for LC and NA are equal in **(a–d)**. The scale in **(e)** and **(f)** is 1 order of magnitude larger for NA compared to LC.

the bedrock of LC (see Fig. 2). High clay contents can be detected in the uppermost meter of the NA profile (partly >20 wt %), and the identified mineral content of the soil pit samples differs significantly from the mineral content of the investigated bedrock (Fig. 7e). The plagioclase (Ca–albite) content distinctly decreases from the bottom of the profile towards the surface and the bedrock content of ~ 28 wt % partly decreases down to 1 wt % in the soil pit. The microcline content on the other hand is relatively uniform. Just as in LC, the chlorite of the bedrock analyzed here (~ 1 wt %) is completely weathered in the NA soil pit profile and is absent from the samples.

The mineral content of the clay-size fraction in LC differs significantly from that in NA (Fig. 8). La Campana is characterized by abundant expandable clay minerals (interstratified chlorite–smectite and interstratified mica–smectite) which can largely be traced back to the weathering of chlorite and biotite (Fig. 8a). Kaolinite can be found throughout the LC profile, whereas interstratified mica–vermiculite only occurs in the depth interval of the discontinuity (120–140 cm; see Fig. 1d). The expandable portion of the interstratified minerals gradually decreases from the profile bottom towards the surface and cannot be detected in the uppermost centimeters of the LC profile. Only mica and kaolinite constitute the clay-size fraction of the uppermost part of the profile in LC. The mineral content in the clay-size fraction of NA is characterized by small amounts of interstratified mica–vermiculite below a depth of 1 m and ubiquitous kaolinite, which shows small expandable portions below a depth of 2 m. Hydroxy-interlayered vermiculite (HIV) and gibbsite can first be detected in 400–450 cm depth and the content increases towards the surface. The main minerals of the clay-size fraction in the uppermost part of the profile are HIV, kaolinite, and gibbsite (Fig. 8b).

5 Discussion

5.1 Climate-dependent mineral transformations

Chemical depletion and mineral transformations are far more pronounced in the profile of NA compared to the profile of LC, even though the bedrock of LC contains more minerals with higher solubility compared to NA (more plagioclase, biotite, chlorite, or hornblende in LC than in NA where quartz and potassium feldspar dominate; see e.g., Wilson, 2004; Bandstra et al., 2008). The high chemical depletion (τ[Na, Ca] up to -0.9 and ΔCIA up to 22; Fig. 5) and the occurrence of gibbsite in NA are indicative of distinct dissolution of primary minerals (especially plagioclase; Fig. 7e) and solute removal of alkali and alkaline earth metals, while im-

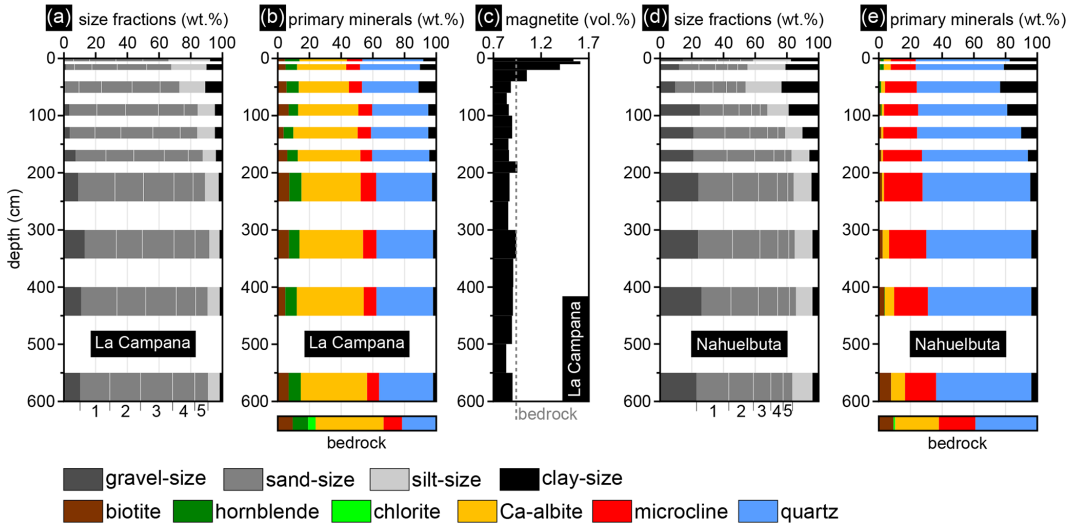

Figure 7. Sieving and pipetting results, semiquantitative XRD results, and approximated magnetite contents of the investigated soil pit samples in La Campana (LC) and Nahuelbuta (NA). **(a)** Grain size distribution based on wet sieving and pipetting, **(b)** semiquantitative XRD, and **(c)** magnetic susceptibility results converted to approximate magnetite contents of the LC profile. **(d)** Wet sieving combined with pipetting results and **(e)** semiquantitative XRD results of the NA samples. Semiquantitative XRD results of the investigated bedrock samples (see Fig. 2) are given below the results of the soil pit samples. In panels **(a)** and **(d)**, 1: ≤2000 to > 1000 µm, 2: ≤ 1000 to > 500 µm, 3: ≤ 500 to > 250 µm, 4: ≤ 250 to > 125 µm, 5: ≤ 125 to > 63 µm.

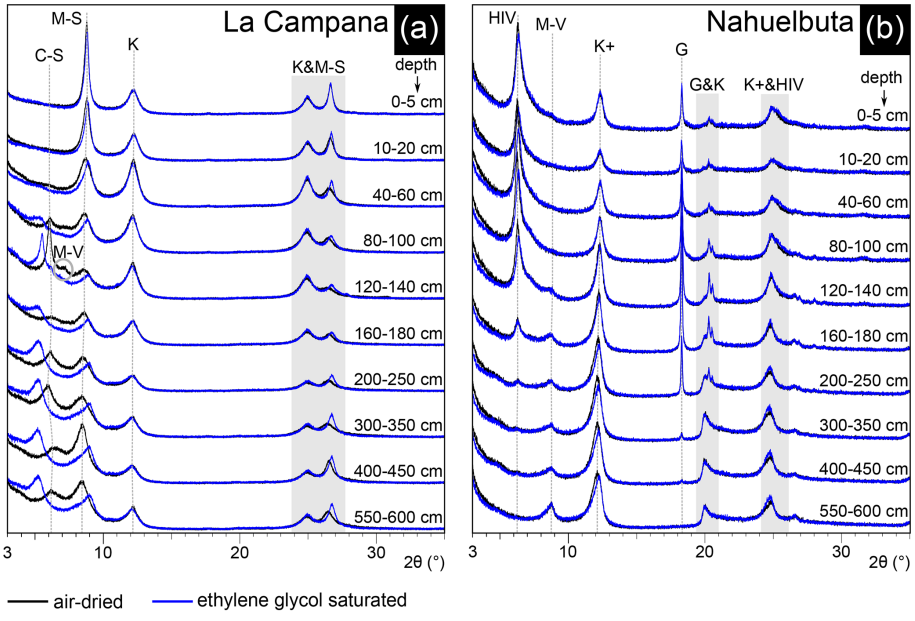

Figure 8. Minerals in the clay-size fraction of the soil pit profiles in La Campana (LC) and Nahuelbuta (NA). **(a)** The profile in LC features abundant expandable clay minerals. **(b)** NA is characterized by the presence of gibbsite and vermiculite but very minor amounts of expandable clay minerals. C–S denotes interstratified chlorite–smectite, G denotes gibbsite, HIV denotes hydroxy-interlayered vermiculite, K denotes kaolinite, K+ denotes kaolinite with expandable portions, M–S denotes interstratified mica–smectite, and M–V denotes interstratified mica–vermiculite.

mobile Al remains as hydroxide ($Al(OH)_3$ = gibbsite). This depletion is assumed to be the result of more water infiltration into the subsurface of NA (more precipitation due to humid climate) compared to LC (less precipitation due to the Mediterranean climate). The measured τ[P] distribution in NA is a clear indication of biologically controlled nutrient uplift and recycling within the topsoil (Jobbágy and Jackson, 2004). We assume that the high precipitation rate in NA leads to more biomass production by plants, which in turn implies more litter production and a stimulation of biogenic decay that supplies plants with nutrients. Thus, we concur with the hypothesis that the ecosystem in NA is thriving on nutrient recycling rather than on an uptake of nutrients that were released by biogenic weathering at depth (Oeser and von Blanckenburg, 2020). Apart from Ca, Na, and P (τ values in Fig. 5), the chemical depletion successively decreases from the surface towards the bottom part of the investigated profile in NA. To account for this shallow chemical depletion, we propose that a secondary-mineral-controlled impeding of the fluid infiltration to depth plays an important role for the depth of mineral transformations in NA.

Chemical depletion can be detected throughout the investigated profile in LC, but the chemical weathering degree is very low between 2–6 m depth (Fig. 5), and the mineral transformations in this section of the profile are only minor (Fig. 7b). On the other hand, there is proof of distinct mineral dissolution and removal of solutes by the higher magnetic susceptibility values in the uppermost decimeters of the LC profile. This can be related to a residual accumulation of weathering-resistant magnetite while other minerals like plagioclase dissolve. The strong chemical depletion in this part of the profile is also reflected by the low τ and elevated CDF as well as Δ CIA values. To account for the detected weak but deep chemical weathering in LC, we propose that a secondary-mineral-controlled formation of fluid pathways facilitates the fluid infiltration to depth and is thus an important control on the chemical weathering reactions in the subsurface.

The difference between the profiles is also displayed by the oxalate- and dithionite-extractable Fe, Si, and Al contents. While high extractable contents especially within the uppermost 2 m of the NA profile are interpreted to indicate considerable ongoing (recent) transformations of primary to secondary minerals, LC shows comparatively little indications in this regard. This difference underlines the higher degree of mineral transformations in NA compared to LC which is also reflected in the mineral content of the clay-size fraction (see Fig. 9). Oxalate-extractable Al contents frequently exceed dithionite-extractable Al contents which is indicative of amorphous phases since oxalate is more effective at extracting amorphous forms of Al (McKeague and Day, 1966). Moreover, the highest contents of the clay-size fraction in the profiles are in good correlation with the elevated extractable Fe, Si, and Al contents and highlight the pronounced mineral transformation in the uppermost part of the profiles. This size fraction hosts most of the products of primary silicate weathering. Clay-size minerals of NA mainly correspond to distinct weathering of plagioclase and biotite, whereas in LC, they can mainly be associated with chlorite and biotite weathering (Fig. 9). Feldspar weathers to kaolinite and gibbsite in NA and biotite weathers to hydroxy-interlayered vermiculite (HIV). Chlorite completely dissolved in the NA profile, whereas both chlorite and biotite in LC weather via interstratified clay minerals to smectite. Finally, smectite and feldspar likely weather to kaolinite in LC (Fig. 9). The mineral composition of the clay-size fraction (Fig. 8) is dependent on the bedrock composition (e.g., more chlorite in LC) and the climate-dependent mineral dissolution (see Fig. 9) in the study sites. However, we argue that the amount of secondary minerals is largely a function of the climatic conditions that control the weathering intensity via water availability in the study sites.

As this study does not consider the entire weathering profile in LC and NA, the interplay between erosion rate and weathering advance rate (Lebedeva and Brantley, 2020) is not addressed here. However, the different denudation rates in the study areas (mean soil denudation rate in LC: ~ 61, in NA: $\sim 33\,\mathrm{t\,km^{-2}\,yr^{-1}}$; Oeser et al., 2018) likely affect the weathering intensity. Due to the higher denudation rates in LC compared to NA (Oeser et al., 2018; van Dongen et al., 2019), we hypothesize that the residence time of weathered material in the regolith of LC is shorter than in NA. Thus, there is less time for chemical weathering in LC. In combination with the lower water availability in LC, this factor might contribute to the lower weathering intensity in the regolith of LC compared to NA. This would also concur with the finding that water availability in the soil and soil residence time are the limiting factors for weathering processes in dry environments (Schoonejans et al., 2016). NA, on the other hand, is characterized by a longer residence time of weathered material. Together with the higher water availability, this factor might contribute to the high weathering intensity in the upper regolith of NA. The situation in LC may be comparable to an incompletely developed profile, while the situation in NA may be comparable to a completely developed profile (Reis and Brantley, 2019).

5.2 Weathering-intensifying processes

5.2.1 Porosity increase by weathering-induced fracturing and its impact on the weathering depth

Ferrous primary minerals of the LC granodiorite can frequently be identified as initiating locations of microcracks. This observation can be related to weathering-induced fracturing (WIF) due to the increase in volume caused by the oxidation of Fe(II) in Fe(II)-bearing silicates (e.g., Buss et al., 2008; Behrens et al., 2015; Kim et al., 2017) and the formation of secondary Fe(III) oxyhydroxides (Fletcher et al., 2006; Lebedeva et al., 2007; Anovitz et al., 2021; Fig. 3d).

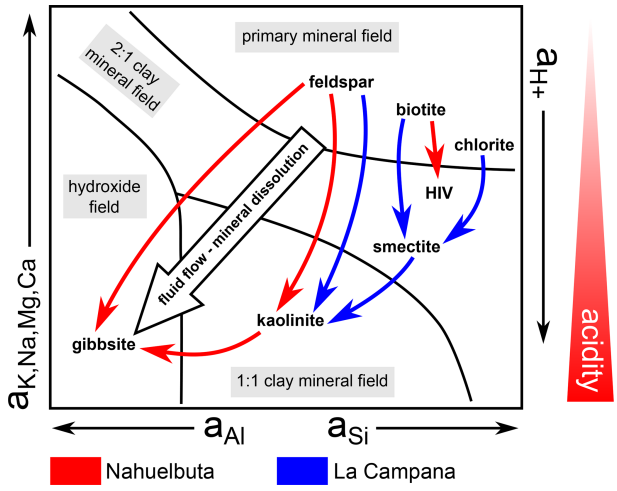

Figure 9. Schematic diagram showing the transformation of primary minerals to secondary minerals (clay minerals and aluminum hydroxide) depending on the activities of H+, Si, Al, K, Na, Mg, and Ca. The depletion of the alkali and alkaline earth metals as well as the increase of the Al activity are coupled to an increase of the mineral dissolution and the removal of solutes by a higher subsurface fluid flow. Elevated a_{H+} values (i.e., lower pH) increase the mineral solubility. Modified from Chesworth et al. (2008). HIV denotes hydroxy-interlayered vermiculite and "a" denotes thermodynamic activity

This process generates and increases surface areas of primary minerals and in turn accelerates weathering reactions (positive feedback between the formation of secondary minerals and the infiltration of fluids (especially O_2 and water) to depth; e.g., Røyne et al., 2008). These weathering-induced fractures consequently facilitate the presence of surface-derived O_2 in the deep subsurface (Kim et al., 2017) and the corresponding transport through the saprolite and soil is dominated by advection (Lebedeva et al., 2007). The bedrock of LC is richer in Fe-bearing minerals than the investigated granite of NA (ca. 25 wt % in LC and ca. 10 wt % in NA) and hosts biotite, hornblende, chlorite, and magnetite as Fe(II) sources. A considerable amount of the total Fe content is bound in magnetite (roughly 0.7 wt % of the total Fe_2O_3 content if the magnetite content of the bulk sample is 1 wt %). However, we found no microscopic evidence (no oxidation) nor indications in the magnetic susceptibility results that the Fe(II) in magnetite is available for weathering reactions. Thus, we conclude that magnetite is stable under the environmental conditions of LC. Of the three remaining Fe(II)-bearing minerals, biotite was found to be the most important one for the generation of WIF in LC (see also Buss et al., 2008; Bazilevskaya et al., 2013, 2015) due to its volumetric expansion during weathering (e.g., Goodfellow et al., 2016). Although WIF also occurs in NA (Fig. 4b), it does not seem to significantly increase the permeability of the rock which can be related to the low Fe(II) content of the dominant bedrock (Fe_2O_3 (total Fe): < 3 wt %; Table S1; see Kim et al., 2017).

Other than that, chlorite is suggested to be an important mineral in the development of the investigated weathering profile in LC. The original chlorite content of the bedrock in LC has been completely transformed into interstratified chlorite–smectite in the soil pit profile. We suggest that this transformation plays a significant role for the development of the LC profile since expandable clay minerals are known to disaggregate rock by swelling (e.g., Dunn and Hudec, 1966; Jiménez-González et al., 2008). The ensuing fracturing also forms new fluid pathways and new access to reactive surfaces of primary minerals which in turn fosters weathering reactions (positive feedback mechanism; see e.g., Røyne et al., 2008). Even though expandable clay minerals can also cause sealing of the subsurface (Kim et al., 2017), we do not regard this effect as significant for LC since clay contents are very low. However, a minor retardation of the fluid flow from surface to depth due to the expansion of the interstratified clay minerals in LC (Fig. 8a) cannot be excluded (see Kim et al., 2017). In conclusion, we propose that small amounts of expandable clay minerals like in LC can generate porosity, whereas high amounts of expandable clay minerals can reduce porosity.

The feedback mechanism of weathering-induced fracturing is presented here for granodiorite. However, the significance of this mechanism is not restricted to plutonic rocks. Weathering-induced fracturing requires Fe(II)-bearing minerals such as biotite and/or potentially the presence of expandable clay minerals that cause the formation of cracks by volume increase during weathering. This feedback concept is thus transferable to all igneous, metamorphic, and sedimentary rocks that contain these minerals.

5.2.2 Increase of weathering intensity by biogenic activity

The formation of secondary minerals such as clay minerals and aluminum hydroxide is among other factors controlled by biogenic activity since organic acids and an acidity increase by elevated organic-derived CO_2 contents accelerate dissolution rates of primary minerals (see e.g., Lucas, 2001; Lawrence et al., 2014). This effect needs to be considered for the organic-rich and acidic subsurface of NA (see Bernhard et al., 2018). The acidity likely contributes to the high degree of mineral dissolution in NA (see a_{H+} in Fig. 9), which consequently leads to an increased formation of secondary minerals.

The depth interval of 120–140 cm in LC is characterized by lower amounts of biotite and a different clay mineral composition compared to the surrounding depth intervals (Figs. 7b, 8a). This depth interval coincides with a discontinuity crossing the entire profile width (Fig. 1d). We interpret this plant-root-containing discontinuity in the saprolite as a fracture remnant since there are no indications of

a lithological heterogeneity in this zone (e.g., a significant change in the magnetic susceptibility or of the primary mineral content; Fig. 7b, c). To explain the lower biotite content and the different clay composition in this part of the profile, we propose an intensification of weathering reactions in the vicinity of the fracture fostered by the observed plant roots (e.g., Fimmen et al., 2008; Pawlik et al., 2016; Nascimento et al., 2021). This weathering-promoting mechanism might account for the increase in interstratified chlorite–smectite and the appearance of interstratified mica–vermiculite (Fig. 8a), while the amount of biotite decreases due to its transformation to secondary minerals (Fig. 7b).

5.3 Weathering-mitigating processes

5.3.1 O_2 consumption by Fe-bearing silicates and its impact on the weathering depth and intensity

The granodiorite of LC hosts an abundance of Fe(II)-bearing minerals (Fig. 7b). The Fe_2O_3 content of the LC bedrock after subtraction of the inert magnetite-bound Fe_2O_3 fraction (since 100 % pure magnetite contains 69 % Fe_2O_3, 0.94 % magnetite as analyzed in the LC bedrock equals 0.65 % magnetite-bound Fe_2O_3 which needs to be subtracted) is 5.34 wt % (for comparison: 2.33 wt % Fe_2O_3 in NA). Since O_2 is reduced by the oxidation of mineral-bound Fe(II) (e.g., White and Yee, 1985; Perez et al., 2005) and the consequent formation of secondary minerals, the O_2 content and hence oxidative weathering reactions are expected to decrease from surface to depth. A rapid decrease of the O_2 concentration to depth is characteristic for weathering systems in which O_2 transport is dominated by diffusion (Behrens et al., 2015). Given the observed deep fracturing due to Fe(II) oxidation (i.e., WIF) in LC and the consequent deep connectivity between the surface and the subsurface (Kim et al., 2017), the O_2 transport in LC is most likely dominated by advection. As a consequence, diffusive O_2 transport is insignificant in the upper regolith of LC and the O_2 consumption by Fe(II) oxidation is not limiting the regolith depth in LC (compare Bazilevskaya et al., 2013). It has been argued that WIF and thus a thicker regolith is more likely when the ratio pO_2 / pCO_2 in soil water is greater than the ratio of the capacity for O_2 consumption to the capacity for CO_2 consumption in bedrock (Stinchcomb et al., 2018). In the study sites, decomposition of organic matter is restricted to the topsoil, likely because organic matter at depth becomes stabilized against microbial decomposition (Scheibe et al., 2023). Thus, we suggest that the pCO_2 of water in the deeper profile part of LC is low (i.e., pO_2 / pCO_2 is high), and O_2 is not being consumed by organic matter decomposition but is available for Fe(II) oxidation and hence WIF. The WIF-controlled connectivity between the surface and the subsurface results in an O_2 availability for oxidative weathering processes at great depth. On the other hand, the weak chemical weathering in LC is in good agreement with the low precipitation rate ($\sim 350\,mm\,yr^{-1}$; Übernickel et al., 2020). The low precipitation rate entails a small infiltration of water to depth which in turn leads to minor primary mineral dissolution and thus chemical weathering at depth.

The cracks around weathered biotite in the investigated samples of LC are (mainly) filled with Fe(III) oxyhydroxides as revealed by the high Fe enrichment detected in electron microprobe maps (Fig. 3d). Newly formed weathering-induced fractures make the biotite more accessible to surface inputs like water and O_2 which promotes the dissolution of biotite. The solutes formed as a result migrate along the weathering-induced cracks and precipitate in the vicinity of the biotite crystal as secondary phases (Fig. 3c). Thus, we propose that the reactive surface of biotite is partly shielded from weathering reactants (water, O_2) due to the precipitation of secondary minerals (see e.g., Navarre-Sitchler et al., 2015; Vázquez et al., 2016; Gerrits et al., 2020, 2021). Combined with the low subsurface water availability in LC causing a low mineral dissolution degree, this shielding might contribute to the relatively stable biotite content throughout the LC profile (Table S4).

5.3.2 Reduction of weathering intensity and depth by damping of fluid flow

The formation of secondary minerals such as clay minerals (via amorphous and poorly crystalline precursors; see Fig. 6) can decrease the porosity (e.g., Bazilevskaya et al., 2015; Navarre-Sitchler et al., 2015) formed by WIF and dissolution. Al-rich phases were found as precipitates in partly dissolved plagioclase of NA (Fig. 4d–f) and within cracks which can often be identified as weathering-induced cracks. We suggest that the abundant presence of clay minerals and gibbsite in NA restricts the fluid flow through such fractures and pores. The clay-rich zone in the uppermost meter of the NA soil pit profile (around 50 cm depth; Fig. 7d) likely acts as a (partially) shielding horizon (impeding vertical flow of surface inputs to the deep subsurface; see e.g., Lohse and Dietrich, 2005). Clay-rich horizons can therefore influence the dynamics of the subsurface fluid flow and thus mitigate mineral transformations and chemical weathering at depth. At the same time, these conditions foster a long fluid residence time in the upper regolith and thus promote the precipitation of secondary minerals such as clay minerals that may impel the weathering of primary minerals in the upper part of the weathering profile (see Maher, 2010). However, the seasonal sealing of fractures and pore spaces due to an increase of soil moisture and an ensuing clay expansion (Kim et al., 2017) is not assumed for NA as expandable secondary minerals barely occur in the clay-size fraction of NA (Fig. 8b).

The negative feedback mechanism presented here is demonstrated for granite. However, the concept is essentially based on newly formed minerals such as clay minerals that inhibit the subsurface fluid flow by blocking pathways. This feedback mechanism can thus be significant for weathering

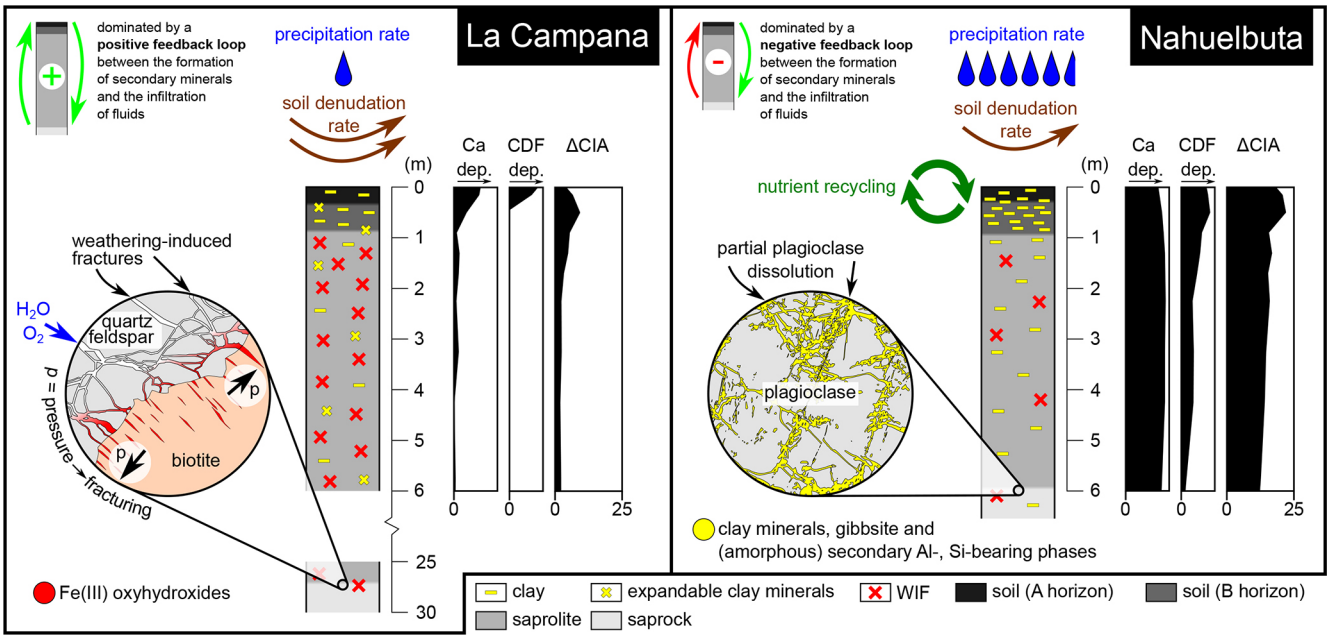

Figure 10. Schematic summary of the two weathering systems. According to our findings, the regolith of La Campana (LC) is dominated by a positive feedback loop between weathering-induced fracturing (WIF) and the infiltration of fluids to depth. WIF creates deep-reaching pathways for fluids (water, O_2) and hence a good connectivity between the surface and the subsurface. Moreover, the low water availability in the Mediterranean climate inhibits the formation of large amounts of secondary minerals (i.e., low weathering intensity) that could seal these pathways. The high denudation rate in LC results in a short residence time of weathered material in the profile and could therefore contribute to the detected lower weathering intensity (i.e., less chemical weathering). The regolith of Nahuelbuta (NA), on the other hand, was found to be dominated by a negative feedback loop between the formation of secondary minerals and amorphous phases and the infiltration of fluids to depth. These secondary solids are consequences of the high water availability in NA that results in intense chemical weathering (i.e., high weathering intensity). The high weathering intensity entails the formation of abundant secondary minerals and amorphous phases that reduce the connectivity between the surface and the subsurface. The lower denudation rate and thus longer residence time of weathered material in NA likely contributes to the more intense chemical weathering; dep. denotes depletion.

systems that develop from all igneous, metamorphic, and sedimentary rocks where secondary minerals can block the permeable porosity formed by WIF and primary mineral dissolution.

6 Conclusions

In two 6 m deep weathering profiles formed on granitic rock in two climatic zones (Mediterranean and humid climate), we found different degrees of elemental loss by chemical weathering and different secondary minerals. Under Mediterranean climate conditions (La Campana), Fe(II) oxidation, precipitation of Fe(III) oxyhydroxide, and clay swelling lead to fracturing and the formation of fluid pathways. This weathering-induced fracturing (WIF) is likely one of the dominant controls in the development of the upper regolith as it leads to a deep infiltration of surface inputs (especially water and O_2) which in turn causes further WIF. While the intensity of chemical weathering at the Mediterranean site is low, it was detected throughout the entire 6 m deep profile. This suggests that the weathering front is located at much greater depth in La Campana. The overall low abundance of secondary minerals can be explained by the low climate-related subsurface water availability in La Campana. The lack of large quantities of secondary minerals ensures that fractures and porosity generated by WIF remain accessible to water and gases. Thus, we conclude that the development of the deep but weak chemical weathering in the upper regolith of La Campana is significantly controlled by two mechanisms: (1) a positive feedback loop between the formation of secondary minerals and the infiltration of fluids to depth induced by (mainly) biotite weathering (WIF) which leads to a deep surface–subsurface connectivity for weathering reactants (in particular O_2) and (2) low subsurface water availability resulting in a low amount of secondary minerals which would otherwise seal this connectivity.

Under humid climate conditions (Nahuelbuta), clay minerals, gibbsite as well as amorphous and poorly crystalline secondary minerals largely formed due to intense plagioclase dissolution. We link this intense dissolution to the high climate-related subsurface water availability in Nahuelbuta. It is suggested that the secondary minerals impede the flow of surface inputs to depth. Moreover, the generally lower amount of Fe(II)-bearing silicates in Nahuelbuta compared

to La Campana results in less WIF and thus fewer fluid pathways. Therefore, we conclude that the development of the weathering profile in Nahuelbuta is predominantly governed by two mechanisms: (1) considerable climate-related subsurface water availability and high biogenic activity which lead to intense weathering of primary minerals in the upper part of the regolith and (2) a negative feedback loop between the formation of secondary minerals and the infiltration of fluids to depth induced by (mainly) plagioclase weathering and the ensuing formation of secondary minerals which leads to a poor surface–subsurface connectivity for weathering reactants. The main findings and factors that are most relevant to the development of the different weathering systems are summarized in Fig. 10.

The relationship between precipitation and the degree of chemical weathering along the climate gradient of the Chilean Coastal Cordillera was found to be non-linear and non-systematic (Oeser and von Blanckenburg, 2020; Schaller and Ehlers, 2022). We argue that a systematic relationship is likely concealed by variations in the mineral content of the bedrock and the associated feedback mechanisms. However, the investigated feedbacks provide a causal explanation for the depth of chemical weathering. This study illustrates how the formation of secondary minerals and the infiltration of surface-derived fluids to depth are interlinked by positive and negative feedback loops. We demonstrated that these feedback loops and the climatic conditions they occur under are important controls in the development of the upper regolith.

Data availability. Datasets related to this article can be found in the data publication Hampl et al. (2022b) (https://doi.org/10.5880/fidgeo.2022.035). The data publication is hosted at the GFZ Data Services and can be downloaded by clicking on "Download data and description" in the field "Files".

Sample availability. The IGSN-registered samples used in this article are deposited at the Department of Applied Geochemistry (Technische Universität Berlin) and are listed in the data publication of this paper (https://doi.org/10.5880/fidgeo.2022.035, Hampl et al., 2022b).

Author contributions. FJH: conceptualization, methodology, investigation, writing – original draft preparation. FS: methodology, supervision, writing – review and editing. CS: investigation, writing – review and editing. NS: investigation, writing – review and editing. CB: funding acquisition, writing – review and editing. FvB: supervision, writing – review and editing. TN: funding acquisition, supervision, writing – review and editing.

Competing interests. The contact author has declared that none of the authors has any competing interests.

Disclaimer. Publisher's note: Copernicus Publications remains neutral with regard to jurisdictional claims in published maps and institutional affiliations.

Special issue statement. This article is part of the special issue "Earth surface shaping by biota (Esurf/BG/SOIL/ESD/ESSD interjournal SI)". It is not associated with a conference.

Acknowledgements. This work was supported by the German Research Foundation (DFG) priority research program SPP-1803 "EarthShape: Earth surface shaping by biota" (grant no. NE 687/9-1) and the EarthShape Coordination (grant nos. EH 329/17-2 and BL562/20-1). We are grateful to Kirstin Übernickel for the management of the drilling campaigns and to Andreas Kappler for his support. We would also like to thank Michael Facklam for his help in determining the clay content and Katja Emmerich for her valuable hints on the clay mineralogy. The authors would also like to thank Peter Finke, Veerle Vanacker, and Susan L. Brantley for their valuable comments and suggestions that greatly improved the paper. Finally, we are grateful to Antonia Roesrath for her help in registering the samples.

Financial support. This research has been supported by the Deutsche Forschungsgemeinschaft (grant no. NE 687/9-1).

This open-access publication was funded
by Technische Universität Berlin.

Review statement. This paper was edited by Veerle Vanacker and reviewed by Susan Brantley, Peter Finke, and Veerle Vanacker.

References

Anderson, S., Dietrich, W., and Brimhall, G.: Weathering profiles, mass-balance analysis, and rates of solute loss: Linkages between weathering and erosion in a small, steep catchment, Geol. Soc. Am. Bull., 114, 1143–1158, https://doi.org/10.1130/0016-7606(2002)114<1143:WPMBAA>2.0.CO;2, 2002.

Anovitz, L. M., Cheshire, M. C., Hermann, R. P., Gu, X., Sheets, J. M., Brantley, S. L., Cole, D. R., Ilton, E. S., Mildner, D. F. R., Gagnon, C., Allard, L. F., and Littrell, K. C.: Oxidation and associated pore structure modification during experimental alteration of granite, Geochim. Cosmochim. Ac., 292, 532–556, https://doi.org/10.1016/j.gca.2020.08.016, 2021.

Bandstra, J. Z., Buss, H. L., Campen, R. K., Liermann, L. J., Moore, J., Hausrath, E. M., Navarre-Sitchler, A. K., Jang, J.-H., and Brantley, S. L.: Compilation of mineral dissolution rates, in: Kinetics of Water-Rock Interaction, edited by: Brantley, S. L., Kubicki, J. D., and White, A. F., Springer New York, 737–823, https://doi.org/10.1007/978-0-387-73563-4, 2008.

Bazilevskaya, E., Lebedeva, M., Pavich, M., Rother, G., Parkinson, D. Y., Cole, D., and Brantley, S. L.: Where fast weathering creates thin regolith and slow weathering cre-

ates thick regolith, Earth Surf. Proc. Land., 38, 847–858, https://doi.org/10.1002/esp.3369, 2013.

Bazilevskaya, E., Rother, G., Mildner, D. F., Pavich, M., Cole, D., Bhatt, M. P., Jin, L., Steefel, C. I., and Brantley, S. L.: How Oxidation and Dissolution in Diabase and Granite Control Porosity during Weathering, Soil Sci. Soc. Am. J., 79, 55–73, https://doi.org/10.2136/sssaj2014.04.0135, 2015.

Behrens, R., Bouchez, J., Schuessler, J. A., Dultz, S., Hewawasam, T., and von Blanckenburg, F.: Mineralogical transformations set slow weathering rates in low-porosity metamorphic bedrock on mountain slopes in a tropical climate, Chem. Geol., 411, 283–298, https://doi.org/10.1016/j.chemgeo.2015.07.008, 2015.

Behrens, R., Wirth, R., and von Blanckenburg, F.: Rate limitations of nano-scale weathering front advance in the slow-eroding Sri Lankan Highlands, Geochim. Cosmochim. Ac., 311, 174–197, https://doi.org/10.1016/j.gca.2021.06.003, 2021.

Bernhard, N., Moskwa, L.-M., Schmidt, K., Oeser, R. A., Aburto, F., Bader, M. Y., Baumann, K., von Blanckenburg, F., Boy, J., van den Brink, L., Brucker, E., Büdel, B., Canessa, R., Dippold, M. A., Ehlers, T. A., Fuentes, J. P., Godoy, R., Jung, P., Karsten, U., Köster, M., Kuzyakov, Y., Leinweber, P., Neidhardt, H., Matus, F., Mueller, C. W., Oelmann, Y., Oses, R., Osses, P., Paulino, L., Samolov, E., Schaller, M., Schmid, M., Spielvogel, S., Spohn, M., Stock, S., Stroncik, N., Tielbörger, K., Übernickel, K., Scholten, T., Seguel, O., Wagner, D., and Kühn, P.: Pedogenic and microbial interrelations to regional climate and local topography: New insights from a climate gradient (arid to humid) along the Coastal Cordillera of Chile, CATENA, 170, 335–355, https://doi.org/10.1016/j.catena.2018.06.018, 2018.

Buss, H. L., Sak, P. B., Webb, S. M., and Brantley, S. L.: Weathering of the Rio Blanco quartz diorite, Luquillo mountains, Puerto Rico: coupling oxidation, dissolution, and fracturing, Geochim. Cosmochim. Ac., 72, 4488–4507, https://doi.org/10.1016/j.gca.2008.06.020, 2008.

Chesworth, W., Camps Arbestain, M., Macías, F., Spaargaren, O., Spaargaren, O., Mualem, Y., Morel-Seytoux, H. J., Horwath, W. R., Almendros, G., Chesworth, W., Grossl, P. R., Sparks, D. L., Spaargaren, O., Fairbridge, R. W., Singer, A., Eswaran, H., Micheli, E., Spaargaren, O., Huang, P. M., and Singer, A.: Clay Mineral Formation, in: Encyclopedia of Soil Science, Encyclopedia of Earth Sciences Series, edited by: Chesworth, W., Springer, Dordrecht, Figure C51, https://doi.org/10.1007/978-1-4020-3995-9_108, 2008.

Dawson, T. E., Hahm, W. J., and Crutchfield-Peters, K.: Digging deeper: what the critical zone perspective adds to the study of plant ecophysiology, New Phytol., 226, 666–671, https://doi.org/10.1111/nph.16410, 2020.

Deckart, K., Hervé, F., Fanning, C., Ramírez, V., Calderón, M., and Godoy, E.: U-Pb Geochronology and Hf-O Isotopes of zircons from the Pennsylvanian Coastal Batholith, South-Central Chile, Andean Geol., 41, 49–82, https://doi.org/10.5027/andgeoV41n1-a03, 2013.

Drever, J. I.: The effect of land plants on weathering rates of silicate minerals, Geochim. Cosmochim. Ac., 58, 2325–2332, https://doi.org/10.1016/0016-7037(94)90013-2, 1994.

Dunn, J. R. and Hudec, P. P.: Water, Clay and Rock Soundness, Ohio J. Sci., 66, 153–168, 1966.

Ferraris, F.: Hoja Los Angeles – Angol, Escala: 1 : 250 000, Carta Geológica de Chile N° 5 (Preliminar), Instituto de Investigaciones Geológicas, OCLC number: 1024799672, 1979.

Ferré, E., Michelsen, K., Ernst, W., Boyd, J., and Cañón-Tapia, E.: Vertical zonation of the Barcroft granodiorite, White Mountains, California: Implications for magmatic processes, Am. Mineral., 97, 1049–1059, https://doi.org/10.2138/am.2012.4013, 2012.

Fimmen, R., Richter, D., Vasudevan, D., Williams, M., and West, L.: Rhizogenic Fe-C redox cycling: A hypothetical biogeochemical mechanism that drives crustal weathering in upland soils, Biogeochemistry, 87, 127–141, https://doi.org/10.1007/s10533-007-9172-5, 2008.

Fletcher, R. C., Buss, H. L., and Brantley, S. L.: A spheroidal weathering model coupling porewater chemistry to soil thicknesses during steady-state denudation, Earth Planet. Sc. Lett., 244, 444–457, https://doi.org/10.1016/j.epsl.2006.01.055, 2006.

Gana, P., Wall, R., and Gutiérrez, A.: Mapa geológico del área de Valparaiso-Curacavi, Región de Valparaiso y Región Metropolitana, Mapas Geológicos, N° 1, Escala 1 : 100 000, Servicio Nacional de Geologia y Mineria (Chile), OCLC number: 43901854, 1996.

Gerrits, R., Pokharel, R., Breitenbach, R., Radnik, J., Feldmann, I., Schuessler, J. A., von Blanckenburg, F., Gorbushina, A. A., and Schott, J.: How the rock-inhabiting fungus K. petricola A95 enhances olivine dissolution through attachment, Geochim. Cosmochim. Ac., 282, 76–97, https://doi.org/10.1016/j.gca.2020.05.010, 2020.

Gerrits, R., Wirth, R., Schreiber, A., Feldmann, I., Knabe, N., Schott, J., Benning, L. G., and Gorbushina, A. A.: High-resolution imaging of fungal biofilm-induced olivine weathering, Chem. Geol., 559, 119902, https://doi.org/10.1016/j.chemgeo.2020.119902, 2021.

Glodny, J., Echtler, H., Collao, S., Ardiles, M., Buron, P., and Figueroa, O.: Differential Late Paleozoic active margin evolution in South-Central Chile (37–40° S) – the Lanalhue Fault Zone, J. S. Am. Earth Sci., 26, 397–411, https://doi.org/10.1016/j.jsames.2008.06.001, 2008a.

Glodny, J., Gräfe, K., Echtler, H., and Rosenau, M.: Mesozoic to Quaternary continental margin dynamics in south-central Chile (36–42° S): The apatite and zircon fission track perspective, Int. J. Earth Sci., 97, 1271–1291, https://doi.org/10.1007/s00531-007-0203-1, 2008b.

Goodfellow, B. W., Hilley, G. E., Webb, S. M., Sklar, L. S., Moon, S., and Olson, C. A.: The chemical, mechanical, and hydrological evolution of weathering granitoid, J. Geophys. Res.-Earth, 121, 1410–1435, https://doi.org/10.1002/2016JF003822, 2016.

Hampl, F. J., Schiperski, F., Byrne, J. M., Schwerdhelm, C., Kappler, A., Bryce, C., von Blanckenburg, F., and Neumann, T.: The role of iron-bearing minerals for the deep weathering of a hydrothermally altered plutonic rock in semi-arid climate (Chilean Coastal Cordillera), Chem. Geol., 604, 120922, https://doi.org/10.1016/j.chemgeo.2022.120922, 2022a.

Hampl, F. J., Schiperski, F., Schwerdhelm, C., Stroncik, N., Bryce, C., von Blanckenburg, F., and Neumann, T.: Mineralogical and geochemical data of two weathering profiles in a Mediterranean and a humid climate region of the Chilean Coastal Cordillera, GFZ Data Services [data set], https://doi.org/10.5880/fidgeo.2022.035, 2022b.

Hayes, N. R., Buss, H. L., Moore, O. W., Krám, P., and Pancost, R. D.: Controls on granitic weathering fronts in contrasting climates, Chem. Geol., 535, 119450, https://doi.org/10.1016/j.chemgeo.2019.119450, 2020.

Hellmann, R., Wirth, R., Daval, D., Barnes, J.-P., Penisson, J.-M., Tisserand, D., Epicier, T., Florin, B., and Hervig, R. L.: Unifying natural and laboratory chemical weathering with interfacial dissolution–reprecipitation: A study based on the nanometer-scale chemistry of fluid–silicate interfaces, Chem. Geol., 294–295, 203–216, https://doi.org/10.1016/j.chemgeo.2011.12.002, 2012.

Hervé, F.: Petrology of the crystalline basement of the Nahuelbuta Mountains, southcentral Chile, in: Comparative Studies on the Geology of the Circum-Pacific Orogenic Belt in Japan and Chile, edited by: Ishikawa, T. and Aguirre, I., Japan Society for the Promotion of Science, Tokyo, 1–51, 1977.

Holbrook, S., Marcon, V., Bacon, A., Brantley, S., Carr, B., Flinchum, B., Richter, D., and Riebe, C.: Links between physical and chemical weathering inferred from a 65-m-deep borehole through Earth's critical zone, Sci. Rep.-UK, 9, 4495, https://doi.org/10.1038/s41598-019-40819-9, 2019.

Holmgren, G. G. S.: A Rapid Citrate-Dithionite Extractable Iron Procedure, Soil Sci. Soc. Am. J., 31, 210–211, https://doi.org/10.2136/sssaj1967.03615995003100020020x, 1967.

Hynek, S., Comas, X., and Brantley, S. L.: The effect of fractures on weathering of igneous and volcaniclastic sedimentary rocks in the Puerto Rican tropical rain forest, Proced. Earth Plan. Sc., 17, 972–975, https://doi.org/10.1016/j.proeps.2017.01.001, 2017.

Israeli, Y., Salhov, E., and Emmanuel, S.: Impact of textural patterns on modeled rock weathering rates and size distribution of weathered grains, Earth Surf. Proc. Land., 46, 1177–1187, https://doi.org/10.1002/esp.5093, 2021.

Jiménez-González, I., Rodríguez-Navarro, C., and Scherer, G. W.: Role of clay minerals in the physicomechanical deterioration of sandstone, J. Geophys. Res., 113, F02021, https://doi.org/10.1029/2007JF000845, 2008.

Jobbágy, E. G. and Jackson, R. B.: The uplift of soil nutrients by plants: biogeochemical consequences across scales, Ecology, 85, 2380–2389, https://doi.org/10.1890/03-0245, 2004.

Kim, H., Stinchcomb, G., and Brantley, S.: Feedbacks among O_2 and CO_2 in deep soil gas, oxidation of ferrous minerals, and fractures: A hypothesis for steady-state regolith thickness, Earth Planet. Sc. Lett., 460, 29–40, https://doi.org/10.1016/j.epsl.2016.12.003, 2017.

Kogure, T. and Banfield, J. F.: New insights into the mechanism for chloritization of biotite using polytype analysis, Am. Mineral., 85, 1202–1208, https://doi.org/10.2138/am-2000-8-913, 2000.

Krone, L. V., Hampl, F. J., Schwerdhelm, C., Bryce, C., Ganzert, L., Kitte, A., Übernickel, K., Dielforder, A., Aldaz, S., Oses-Pedraza, R., Perez, J. P. H., Sanchez-Alfaro, P., Wagner, D., Weckmann, U., and von Blanckenburg, F.: Deep weathering in the semi-arid Coastal Cordillera, Chile, Sci. Rep.-UK, 11, 13057, https://doi.org/10.1038/s41598-021-90267-7, 2021.

Lawrence, C., Harden, J., and Maher, K.: Modeling the influence of organic acids on soil weathering, Geochim. Cosmochim. Ac., 139, 487–507, https://doi.org/10.1016/j.gca.2014.05.003, 2014.

Lebedeva, M. I. and Brantley, S. L.: Exploring an "ideal hill": how lithology and transport mechanisms affect the possibility of a steady state during weathering and erosion, Earth Surf. Proc. Land., 45, 652–665, https://doi.org/10.1002/esp.4762, 2020.

Lebedeva, M. I., Fletcher, R. C., Balashov, V. N., and Brantley, S. L.: A reactive diffusion model describing transformation of bedrock to saprolite, Chem. Geol., 244, 624–645, https://doi.org/10.1016/j.chemgeo.2007.07.008, 2007.

Lohse, K. A. and Dietrich, W. E.: Contrasting effects of soil development on hydrological properties and flow paths, Water Resour. Res., 41, W12419, https://doi.org/10.1029/2004WR003403, 2005.

Lucas, Y.: The Role of Plants in Controlling Rates and Products of Weathering: Importance of Biological Pumping, Annu. Rev. Earth Pl. Sc., 29, 135–163, https://doi.org/10.1146/annurev.earth.29.1.135, 2001.

Luebert, F. and Pliscoff, P.: Sinópsis bioclimática y vegetacional de Chile, Editorial Universitaria, Santiago de Chile, ISBN 956-11-1832-7, 2006.

Maher, K.: The dependence of chemical weathering rates on fluid residence time, Earth Planet. Sc. Lett., 294, 101–110, https://doi.org/10.1016/j.epsl.2010.03.010, 2010.

McKeague, J. A. and Day, J. H.: Dithionite- and oxalate-extractable Fe and Al as aids in differentiating various classes of soils, Can. J. Soil Sci., 46, 13–22, https://doi.org/10.4141/cjss66-003, 1966.

Melnick, D.: Rise of the central Andean coast by earthquakes straddling the Moho, Nat. Geosci., 9, 401–407, https://doi.org/10.1038/ngeo2683, 2016.

Molnar, P., Anderson, R. S., and Anderson, S. P.: Tectonics, fracturing of rock, and erosion, J. Geophys. Res., 112, F03014, https://doi.org/10.1029/2005JF000433, 2007.

Nadan, B. J. and Engelder, T.: Microcracks in New England granitoids: A record of thermoelastic relaxation during exhumation of intracontinental crust, Geol. Soc. Am. Bull., 121, 80–99, https://doi.org/10.1130/b26202.1, 2009.

Napieralski, S. A., Buss, H. L., Brantley, S. L., Lee, S., Xu, H., and Roden, E. E.: Microbial chemolithotrophy mediates oxidative weathering of granitic bedrock, P. Natl. Acad. Sci. USA, 116, 26394–26401, https://doi.org/10.1073/pnas.1909970117, 2019.

Nascimento, D. L., Abrahão, A., Lambers, H., Teodoro, G. S., Ladeira, F. S. B., de Britto Costa, P., Oliveira, R. S., and de Farias, C. H. B.: Biogeomorphological evolution of rocky hillslopes driven by roots in campos rupestres, Brazil, Geomorphology, 395, 107985, https://doi.org/10.1016/j.geomorph.2021.107985, 2021.

Navarre-Sitchler, A., Brantley, S. L., and Rother, G.: How Porosity Increases During Incipient Weathering of Crystalline Silicate Rocks, Rev. Mineral. Geochem., 80, 331–354, https://doi.org/10.2138/rmg.2015.80.10, 2015.

Nesbitt, H. and Young, G.: Early Proterozoic climates and plate motions inferred from major element chemistry of lutites, Nature, 299, 715–717, https://doi.org/10.1038/299715a0, 1982.

Oeser, R. A., Stroncik, N, Moskwa, L.-M., Bernhard, N., Schaller, M., Canessa, R., van den Brink, L., Köster, M., Brucker, E., Stock, S., Fuentes, J. P., Godoy, R., Matus, F. J., Oses Pedraza, R., Osses McIntyre, P., Paulino, L., Seguel, O., Bader, M. Y., Boy, J., Dippold, M. A., Ehlers, T. A., Kühn, P., Kuzyakov, Y., Leinweber, P., Scholten, T., Spielvogel, S., Spohn, M., Übernickel, K., Tielbörger, K., Wagner, D., and von Blanckenburg, F.: Chemistry and microbiology of the Critical Zone along a steep climate and vegetation gradient

in the Chilean Coastal Cordillera, CATENA, 170, 183–203, https://doi.org/10.1016/j.catena.2018.06.002, 2018.

Oeser, R. A. and von Blanckenburg, F.: Do degree and rate of silicate weathering depend on plant productivity?, Biogeosciences, 17, 4883–4917, https://doi.org/10.5194/bg-17-4883-2020, 2020.

Pawlik, Ł., Phillips, J. D., and Šamonil, P.: Roots, rock, and regolith: Biomechanical and biochemical weathering by trees and its impact on hillslopes – A critical literature review, Earth-Sci. Rev., 159, 142–159, https://doi.org/10.1016/j.earscirev.2016.06.002, 2016.

Perez, J. R., Banwart, St. A., and Puigdomenech, I.: The kinetics of $O_{2(aq)}$ reduction by structural ferrous iron in naturally occurring ferrous silicate minerals, Appl. Geochem., 20, 2003–2016, https://doi.org/10.1016/j.apgeochem.2005.07.001, 2005.

Reis, F. D. A. A. and Brantley, S. L.: The impact of depth-dependent water content on steady state weathering and eroding systems, Geochim. Cosmochim. Acta, 244, 40–55, https://doi.org/10.1016/j.gca.2018.09.028, 2019.

Rempe, D. M. and Dietrich, W. E.: A bottom-up control on fresh-bedrock topography under landscapes, P. Natl. Acad. Sci. USA, 111, 6576–6581, https://doi.org/10.1073/pnas.1404763111, 2014.

Rennert, T.: Wet-chemical extractions to characterise pedogenic Al and Fe species – a critical review, Soil Res., 57, 1–16, https://doi.org/10.1071/SR18299, 2019.

Riebe, C. S., Kirchner, J. W., and Finkel, R. C.: Long-term rates of chemical weathering and physical erosion from cosmogenic nuclides and geochemical mass balance, Geochim. Cosmochim. Ac., 67, 4411–4427, https://doi.org/10.1016/S0016-7037(03)00382-X, 2003.

Røyne, A., Jamtveit, B., Mathiesen, J., and Malthe-Sørenssen, A.: Controls on rock weathering rates by reaction-induced hierarchical fracturing, Earth Planet. Sc. Lett., 275, 364–369, https://doi.org/10.1016/j.epsl.2008.08.035, 2008.

Schaller, M. and Ehlers, T. A.: Comparison of soil production, chemical weathering, and physical erosion rates along a climate and ecological gradient (Chile) to global observations, Earth Surf. Dynam., 10, 131–150, https://doi.org/10.5194/esurf-10-131-2022, 2022.

Scheibe, A., Sierra, C. A., and Spohn, M.: Recently fixed carbon fuels microbial activity several meters below the soil surface, Biogeosciences, 20, 827–838, https://doi.org/10.5194/bg-20-827-2023, 2023.

Schneider, C. A., Rasband, W. S., and Eliceiri, K. W.: NIH Image to ImageJ: 25 years of image analysis, Nat. Methods, 9, 671–675, https://doi.org/10.1038/nmeth.2089, 2012.

Schoonejans, J., Vanacker, V., Opfergelt, S., Ameijeiras-Mariño, Y., and Christl, M.: Kinetically limited weathering at low denudation rates in semiarid climatic conditions. J. Geophys. Res.-Earth., 121, 336–350, https://doi.org/10.1002/2015JF003626, 2016.

Schwertmann, U.: Differenzierung der Eisenoxide des Bodens durch Extraktion mit Ammoniumoxalat-Lösung, Zeitschrift für Pflanz., Düngung, Bodenkunde, 105, 194–202, https://doi.org/10.1002/jpln.3591050303, 1964.

Starkey, H. C., Blackmon P. D., and Hauff P. L. The routine mineralogical analysis of clay-bearing samples, U.S. Geological Survey Bulletin, 1563, https://doi.org/10.3133/b1563, 1984.

St. Clair, J., Moon, S., Holbrook, W. S., Perron, J. T., Riebe, C. S., Martel, S. J., Carr, B., Harman, C., Singha, K., and Richter, D.: Geophysical imaging reveals topographic stress control of bedrock weathering, Science, 350, 534–538, https://doi.org/10.1126/science.aab2210, 2015.

Steefel, C. I. and van Cappellen, P.: A new kinetic approach to modeling water-rock interaction: The role of nucleation, precursors, and Ostwald ripening, Geochim. Cosmochim. Ac., 54, 2657–2677, https://doi.org/10.1016/0016-7037(90)90003-4, 1990.

Steenken, A., Rabbia, O., and Hernández, L.: The Emplacement of the Nahuelbuta Batholith in an Active Continental Margin (Central Chile), XVIII Congreso Peruano de Geología, Lima, Peru, 16–19 October 2016, 2016.

Stinchcomb, G. E., Kim, H., Hasenmueller, E. A., Sullivan, P. L., Sak, P. B., and Brantley, S. L.: Relating soil gas to weathering using rock and regolith geochemistry, Am. J. Sci., 318, 727–763, https://doi.org/10.2475/07.2018.01, 2018.

Übernickel, K., Ehlers, T. A., Ershadi, M. R., Paulino, L., Fuentes Espoz, J.-P., Maldonado, A., Oses-Pedraza, R., and von Blanckenburg, F.: Time series of meteorological station data in the EarthShape study areas in the Coastal Cordillera, Chile, GFZ Data Services [data set], https://doi.org/10.5880/fidgeo.2020.043, 2020.

van Dongen, R., Scherler, D., Wittmann, H., and von Blanckenburg, F.: Cosmogenic ^{10}Be in river sediment: where grain size matters and why, Earth Surf. Dynam., 7, 393–410, https://doi.org/10.5194/esurf-7-393-2019, 2019.

Vázquez, M., Ramírez, S., Morata, D., Reich, M., Braun, J.-J., and Carretier, S.: Regolith production and chemical weathering of granitic rocks in central Chile, Chem. Geol., 446, 87–98, https://doi.org/10.1016/j.chemgeo.2016.09.023, 2016.

Werner, C., Schmid, M., Ehlers, T. A., Fuentes-Espoz, J. P., Steinkamp, J., Forrest, M., Liakka, J., Maldonado, A., and Hickler, T.: Effect of changing vegetation and precipitation on denudation – Part 1: Predicted vegetation composition and cover over the last 21 thousand years along the Coastal Cordillera of Chile, Earth Surf. Dynam., 6, 829–858, https://doi.org/10.5194/esurf-6-829-2018, 2018.

White, A. F. and Yee, A.: Aqueous oxidation-reduction kinetics associated with coupled electron transfer from iron-containing silicates at 25° C, Geochim. Cosmochim. Ac., 49, 1263–1275, https://doi.org/10.1016/0016-7037(85)90015-8, 1985.

Wilson, M. J.: Weathering of the primary rock-forming minerals: processes, products and rates, Clay Miner., 39, 233–266, https://doi.org/10.1180/0009855043930133, 2004.